Mid-Infrared Frequency Comb Generation and Spectroscopy with Few-Cycle Pulses and $\chi^{(2)}$ Nonlinear Optics

Alexander J. Lind,[1,2,†,‡] Abijith Kowligy,[1,2,‡] Henry Timmers,[1,‡] Flavio C. Cruz,[1,3] Nima Nader,[4]
Myles C. Silfies,[5] Thomas K. Allison[5] and Scott A. Diddams[1,2,*]

[1]*Time and Frequency Division, National Institute of Standards and Technology, 325 Broadway, Boulder, Colorado 80305, USA*
[2]*Department of Physics, University of Colorado, 2000 Colorado Avenue, Boulder, Colorado 80309, USA*
[3]*Instituto de Fisica Gleb Wataghin, Universidade Estadual de Campinas, Campinas, SP 13083-859, Brazil*
[4]*Applied Physics Division, National Institute of Standards and Technology, 325 Broadway, Boulder, Colorado 80305, USA*
[5]*Department of Chemistry and Physics, Stony Brook University, Stony Brook, New York 11794, USA*

The mid-infrared atmospheric window of 3–5.5 μm holds valuable information regarding molecular composition and function for fundamental and applied spectroscopy. Using a robust, mode-locked fiber-laser source of < 11 fs pulses in the near infrared, we explore quadratic ($\chi^{(2)}$) nonlinear optical processes leading to frequency comb generation across this entire mid-infrared atmospheric window. With experiments and modeling, we demonstrate intrapulse difference frequency generation that yields few-cycle mid-infrared pulses in a single pass through periodically poled lithium niobate. Harmonic and cascaded $\chi^{(2)}$ nonlinearities further provide direct access to the carrier-envelope offset frequency of the near infrared driving pulse train. The high frequency stability of the mid-infrared frequency comb is exploited for spectroscopy of acetone and carbonyl sulfide with simultaneous bandwidths exceeding 11 THz and with spectral resolution as high as 0.003 cm^{-1}. The combination of low noise and broad spectral coverage enables detection of trace gases with concentrations in the part-per-billion range.

DOI: 10.1103/PhysRevLett.124.133904

Laser frequency combs exist at the rich convergence of time and frequency domains, where they simultaneously combine the physics of ultrafast nonlinear optics and high-resolution frequency metrology [1,2]. Advances in comb-generating nonlinear optics draws from diverse fields but have typically focused on the use of the ultrafast third-order nonlinearity ($\chi^{(3)}$) for spectral generation and mode locking of laser sources in the visible and near infrared. While this region of the spectrum has good overlap with the electronic transitions of optical clocks and alkali atoms, frequency combs in the mid-infrared (MIR) enable rovibrational spectroscopy for molecular detection and identification [3]. The infrared atmospheric window at 3–5.5 μm, exhibits reduced attenuation while demonstrating strong absorption coefficients for greenhouse gases and pollutants such as methane, ethane, carbon dioxide, and formaldehyde [4–11], making this spectral range useful for climate research and atmospheric monitoring. Further, the same spectral window contains molecular structure information pertaining to the C-H and O-H functional groups which can be used in the characterization of biochemical molecules [12,13] and spectroimaging of biological samples [14,15]. At the same time, broad bandwidth few-cycle pulsed sources in the MIR are valuable for driving high-harmonic generation and strong-field physics in both gases and solids [16–18].

Based on these motivations, multiple approaches to MIR frequency comb and coherent short pulse generation have been pursued. Examples include optical parametric oscillators (OPOs) [19–23], supercontinuum generation [24–27], difference frequency generation (DFG) [28–31], direct generation with quantum cascade lasers (QCLs) [32–34], mode-locked fiber lasers [35–37], and micro-resonator frequency combs [38]. Despite significant progress, many of these frequency comb sources require additional resonant cavities (OPOs) or careful spatiotemporal alignment of two femtosecond pulses (DFG) that increases complexity. Others lack absolute frequency calibration or have large mode-spacings (microresonator combs and QCLs) that are mismatched to the spectroscopy of small molecules.

In this Letter, we demonstrate a simple and powerful method for generating broadband frequency combs across the 3–5 μm MIR atmospheric window using intrapulse DFG driven by few-cycle pulses within a $\chi^{(2)}$ material [39–41]. With detailed modeling, we show how to engineer the nonlinear interactions in a single pass through a chirped periodically poled crystal to provide three-cycle MIR optical pulses with corresponding simultaneous spectral coverage of 40 THz (1333 cm^{-1}). We avoid the strict requirements of spatiotemporal overlap encountered in conventional DFG sources, eliminating a major source of intensity noise while

enabling long-term robust operation. As an auxiliary benefit, the few-cycle pulse nonlinear optics provides the carrier-envelope offset frequency of the driving pulse train directly, which we use to fully stabilize the near-infrared (NIR) comb spanning 1–2 μm. We employ the MIR comb for dual comb spectroscopy (DCS) [42]. With excellent signal-to-noise ratio (SNR) and the capability to accurately resolve both broad- and narrow-band spectral features, we achieve a sensitivity of 40 ppb · m Hz$^{-1/2}$ for carbonyl sulfide molecules using multiline detection [43].

The experimental setup is shown in Fig. 1(a). In contrast to intrapulse DFG driven by multi-Watt laser systems at 1 and 2 μm [44–48], we employ robust and technologically mature fiber laser technology starting in the 1.55 μm region to pump periodically poled lithium niobate (PPLN). We amplify and spectrally broaden the output of a 100 MHz Er: fiber oscillator to generate 3 nJ few-cycle pulses (10.6 fs, 2.1 cycles) centered at 1.55 μm, as in [39]. In typical experiments, we focus the few-cycle pulse with a 25 mm focal length silver-coated off-axis parabolic (OAP) mirror into 1 mm-long PPLN crystal, achieving a minimum beam diameter of 16 μm. The broadband output of the PPLN crystal is collected with another OAP mirror, optically filtered, and measured on a Fourier transform spectrometer (FTS) or sent to a liquid nitrogen-cooled mercury cadmium telluride (MCT) detector. The spectrum of the few-cycle pump is shown in Fig. 1(b), and it contains sufficient bandwidth ($\approx$100 THz) to support the generation of 3 μm light.

The modes of a frequency comb are defined through two radio frequency parameters, the repetition rate ($f_{\rm rep}$) and the offset frequency (f_0), such that a given mode, n, has optical frequency, $\nu_n = n f_{\rm rep} + f_0$. For DFG, that occurs within the original input pulse, the resulting MIR light will be "offset free," meaning the offset frequency of the comb will subtract out in the DFG process. However, due to the high peak intensities within the crystal, cascaded $\chi^{(2)}$ nonlinear processes give rise to additional comb modes throughout the spectrum with which we observe f_0 in heterodyne beats at multiple wavelengths, as shown in Fig. 1(c). For example, at 600 nm, we observe the $2f$–$3f$ interference, from cascaded quasi-phase-matching (QPM) tripling of 1.8 μm and third-order phase-matched doubling of 1.2 μm. At 900 nm, a f–$2f$ interference results from QPM 1.8 μm frequency doubling beating with slightly broadened comb light. At 3500 nm, we observe an "$f-0$" beat note between the "offset-free" DFG comb, and DFG between doubled light from 2 μm (with a factor of $2f_0$) and the original 1.5 μm comb (containing a single f_0) [49]. We estimate that the power of the f_0 comb is 40 dB smaller than that of the f_0-free comb in the MIR. In subsequent electro-optic sampling experiments [50], the time-domain impact of this small f_0 comb had negligible impact on the phase stable few-cycle waveform associated with the offset-free DFG comb.

We implement optical frequency control by phase-locking a NIR comb tooth to a narrow-linewidth 1.55 μm laser. In addition, we control the offset frequency of the combs by using the f_0 signal detected at 3500 nm with the same MCT detector used for MIR spectroscopy [Fig. 4(a)]. The integrated phase noise on the locked offset frequency is 115 mrad, integrated from 50 Hz to 2 MHz, and comparable to other methods of offset frequency stabilization.
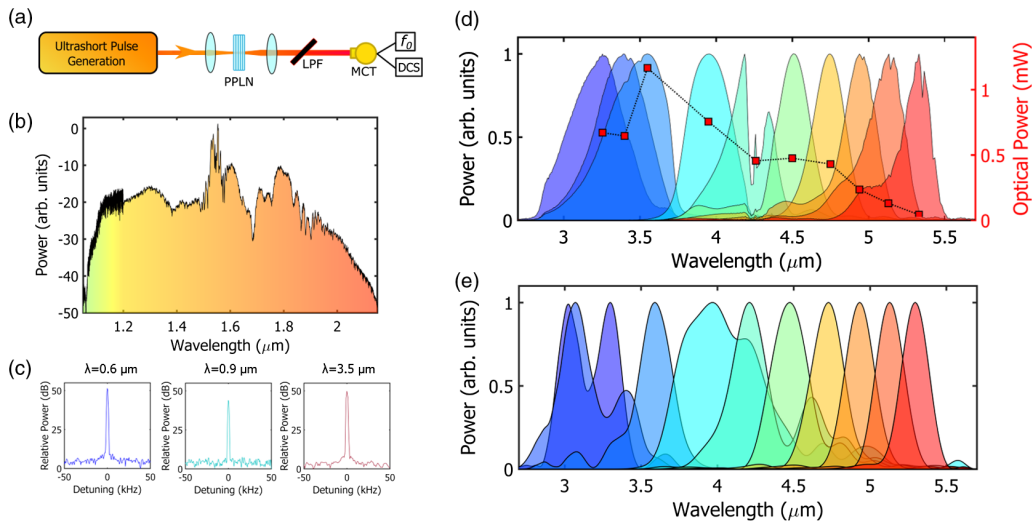

FIG. 1. (a) Experimental setup of MIR generation and offset frequency (f_0) detection. (b) An optical spectrum of the ultrashort pulse. (c) Offset frequency beat notes measured at 600, 900, and 3500 nm (resolution bandwidth, RBW = 1 kHz). (d) Measured intrapulse DFG spectra with a commercial FTS (4 cm^{-1}/120 GHz resolution). All spectra are normalized to the peak signal. The measured power for each spectrum is indicated by the square markers, referencing the axis on the right. Atmospheric CO_2 absorption is visible in the spectrum centered around 4.3 μm. (e) Predicted MIR spectra, also normalized. LPF: Longpass filter.

The PPLN crystal contains a set of discrete poling periods, ranging from $\Lambda = 24.1\text{--}35.6\ \mu m$ in steps of approximately $0.6\ \mu m$. The longer (shorter) poling periods provide QPM for DFG into shorter (longer) wavelengths in the MIR. By tuning across these poling periods, MIR light spans $3\text{--}5.5\ \mu m$ [Fig. 1(d)]. The maximum power measured in the MIR spectra is 1.3 mW. However, on average, these spectra yield approximately 500 μW, which is sufficient to saturate the MCT detectors used in our spectroscopy measurements.

We model the few-cycle pulse interaction within the quadratic nonlinear medium using a nonlinear envelope equation (NEE) that supports studying the ultrabroadband phenomena, including harmonic generation, that we observe experimentally. The NEE is analogous to the nonlinear Schrödinger equation for cubic nonlinear physics [51], and is expressed as

$$\frac{\partial A}{\partial z} + i\hat{D}A(z,t) = i\left(1 + \frac{i}{\omega_0}\frac{\partial}{\partial t}\right)$$
$$\times \chi(z)(A^2 e^{-i\phi(z,t)} + |A|^2 e^{i\phi(z,t)}), \qquad (1)$$

where A is the envelope of the electric field, $\hat{D} = \sum_{j=2}(1/j!)\beta_j[i(\partial/\partial t)]^j$ is the dispersion operator, $\chi(z) = \chi^{(2)}(z)\omega_0^2/4\beta_0 c^2$ accounts for periodic poling and the nonlinear susceptibility, $\phi(z,t) = \omega_0 t - (\beta_0 - \beta_1\omega_0)z$, and β_j are the coefficients of a Taylor expansion of $\beta(\omega) = \omega n(\omega)/c$, the propagation constant, about ω_0 [52]. In the second line of the equation, the first term accounts for harmonic and sum frequency generation, while the second term is responsible for difference frequency generation or optical rectification. We numerically integrate Eq. (2) to model the propagation of a few-cycle pulse centered at 1.55 μm through a 1-mm PPLN crystal, subject to a Gaussian focusing profile, with results summarized in Fig. 1(e). The locations of the spectral peaks from the model agree well with experimental data, as do the relative bandwidths.

The bandwidth generated (300–500 nm) in the MIR is limited by group velocity dispersion elongating the pulse (112 fs^2/mm at 1.55 μm) and the phasematching bandwidth for a single poling period. Instead, by using crystals with a chirped poling period (aperiodic poling), we show how to significantly increase the QPM bandwidth [53]. To implement a chirped poling period, we use a fan-out PPLN [54] tilted at approximately 45°, such that the pulse experiences different poling periods as it passes through the crystal. Through these chirped grating periods, we generate
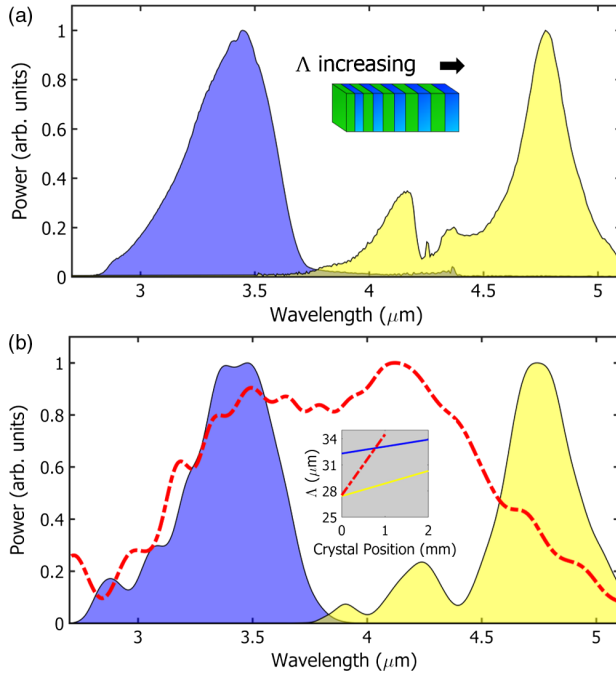

FIG. 2. Broad bandwidth MIR generation. (a) Using a chirped PPLN crystal, we generate broader bandwidth MIR light. The blue and yellow curves correspond to different chirp profiles. CO_2 absorption is also visible in the yellow spectrum at 4.3 μm. Powers for the two spectra are 1.3 mW (blue) and 360 μW (yellow). (b) Modeling of the experimental spectra with chirp profiles shown in the inset. The red dashed line is a modeled profile which covers this full spectral region. The chirp rate for each spectrum is 0.8 $\mu m/mm$ (blue), 1.45 $\mu m/mm$ (yellow), and 7 $\mu m/mm$ (red dashed).
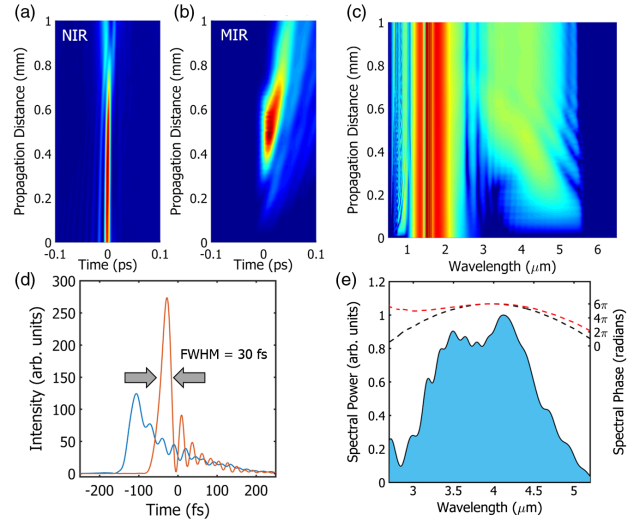

FIG. 3. Simulation results in time and frequency domain for the modeled chirp profile. (a) Time domain propagation of the NIR ultrashort pulse. (b) Time domain propagation of the MIR pulse. (c) Frequency domain propagation. Most light is generated near the middle of the crystal, but some higher frequency components arise near the end of the PPLN. (d) Time domain traces of the MIR pulse at the output of the PPLN (blue) and after 0.5 mm of Ge (red). The transform-limited pulse duration is 20 fs. (e) Left axis: MIR spectrum at the output of the PPLN. Right axis: Spectral phase of the pulse at the output of the PPLN (black dashed) and after 0.5 mm of Ge (red dashed).

bandwidths > 1000 nm [Fig. 2(a)]. The chirp and, thus, the generated bandwidth, is limited by the crystal angle in the current implementation. A chirp of the opposite sign results in a significantly more modulated spectrum. Using Eq. (1) and grating chirp profiles shown in the inset of Fig. 2(b), we reproduce the experimental spectra [Fig. 2(b)]. With an optimized PPLN chirp profile [Fig. 2(b), red dashed line], our modeling shows it is possible to cover the entire 3–5 μm spectral region in a single pass, allowing for the simultaneous probing of many molecular species [22].

Our modeling also illustrates a means for generating ultrashort MIR pulses. We numerically investigate the temporal structure of the MIR comb, using the chirped PPLN profile defined by the red dashed line in Fig. 2(b). We separately Fourier transform the NIR and MIR portions of the spectrum [Fig. 3(c)] at each propagation point to obtain the corresponding temporal intensity profiles [Figs. 3(a) and 3(b)]. The temporal structure of the MIR pulse at the output of the PPLN is shown in blue in Fig. 3(d), with the spectral phase shown in the black dashed line in Fig. 3(e). Our simulations indicate that the pulses can be fairly well compressed simply by propagation through 0.5 mm of bulk Ge [Fig. 3(d), red curve, and

Fig. 3(e), red dashed curve]. This would yield a 30 fs MIR pulse with duration limited by third-order dispersion.

To highlight the stable and tunable nature of the MIR light, we perform gas-phase DCS [42] on acetone and carbonyl sulfide (OCS) using two of these intrapulse DFG sources. Details of the experimental setup are shown in Fig. 4(a). Broad bandwidth spectral stability of the MIR combs, as required for precise absorbance baseline determination, is shown in the infrared spectrum of acetone [Fig. 4(b)]. We fill the gas cell by placing a few drops of liquid acetone into the cell and sealing it, resulting in atmospheric pressure-broadened acetone vapor. We average interferogram acquisitions over approximately five minutes, and time-domain apodization to 200 μs brings the effective resolution to 0.3 cm^{-1} (10 GHz). These data only require a linear baseline correction to agree with the model, provided by the Pacific Northwest National Laboratory (PNNL) Infrared Database [55]. The additional noise on the blue side of the spectrum is due to a power drop off in the optical spectrum.

We benchmark the combined bandwidth, resolution, and sensitivity of our systems with the infrared spectroscopy of a dilute OCS sample (67 μbar OCS in 67 mbar N$_2$) [Figs. 4(c)–4(d)]. A low background pressure in the cell
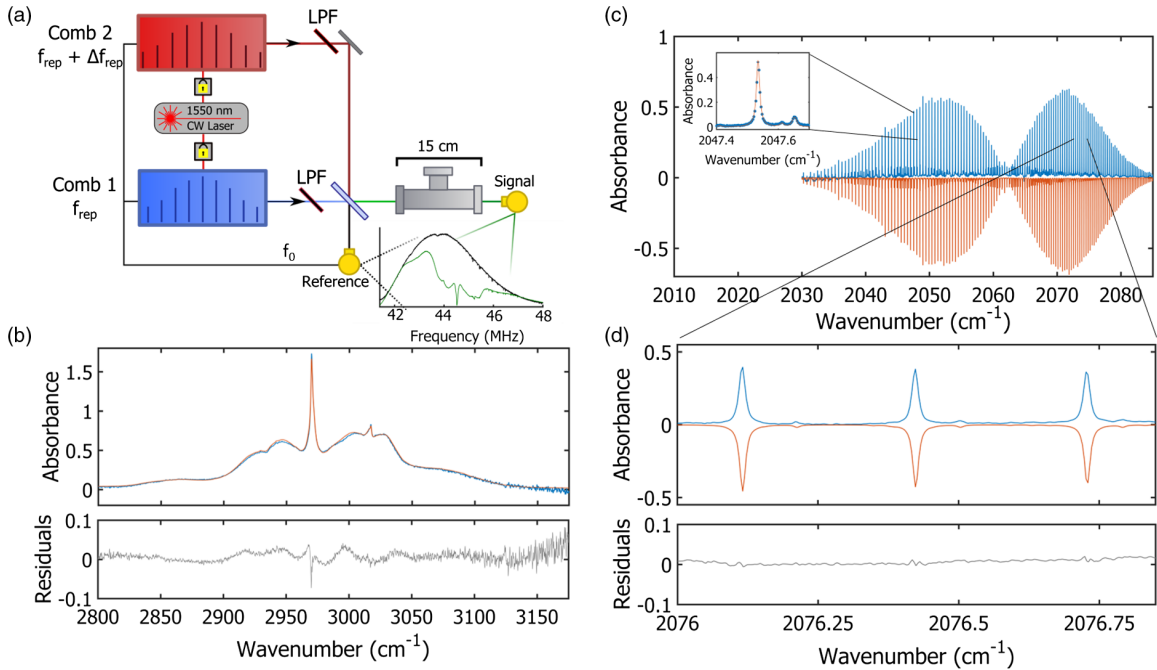

FIG. 4. Dual-comb spectroscopy. (a) Two MIR combs with $\Delta f_{\text{rep}} = 50$ Hz (20 ms interferograms) combine on a 50/50 CaF$_2$ beamsplitter. One combined beam is directly detected on a MCT detector to provide a reference spectrum. The offset frequencies (f_0) are also detected from this detector. By tuning and locking the oscillator f_0 away from the DCS heterodyne that resides in an rf band between 27 and 50 MHz, we avoid interference between the two signals. The other beam is sent through a 15 cm-long gas cell and detected on a second MCT detector. The Fourier transform of the time-domain signal is shown in the inset. (b) Acetone dual comb spectroscopy. Experimental (blue) and predicted (red) spectra. (c), (d) OCS dual-comb spectroscopy. The inset in (c) shows data recorded with comb-tooth resolution. The zoomed-in portion of the OCS data in (d) highlights good agreement over absorbance ranging 0.02 to 0.5 in only 90 seconds of averaging. The small absorption features are evidence of the ^{16}O^{12}C^{34}S isotopologue. CW: continuous wave.

allows us to look at narrow absorption features less impacted by pressure broadening. For these data, we use the full 20 ms interferogram, providing a resolution of 0.003 cm^{-1} (100 MHz), while only averaging over 1.5 minutes of data. The data presented in the inset of Fig. 4(c) averages a string of five consecutive interferograms (100 ms acquisition) to measure with comb-tooth resolution. The model comes from the HITRAN database [56]. We are able to accurately reproduce the spectral envelope [Fig. 4(c)], as well as match individual lines in both magnitude and line center [Fig. 4(d)].

In this measurement, we achieve a peak frequency-domain SNR, normalized to one second of averaging, of 76 Hz$^{1/2}$. Accounting for ≈ 2 THz of optical bandwidth around 2060 cm^{-1}, we find a figure-of-merit, defined as the product of SNR and number of comb teeth, of 1.3×10^6 Hz$^{1/2}$ [42]. For a 15-cm interaction length, this corresponds to a noise-equivalent absorbance of 8.8×10^{-4} cm^{-1} Hz$^{-1/2}$. With this performance, the minimum detectable concentration of OCS is 40 ppb $\cdot$ m Hz$^{-1/2}$, taking into account the enhancement in sensitivity due to measuring many features simultaneously [43]. This is comparable with other recent measurements in this wavelength region [22,30,57]. Our demonstrated sensitivity is particularly compelling, especially when accounting for the large optical bandwidths, short interaction length, and small footprint (<0.25 m^2) employed here in contrast to prior work.

In summary, we used the $\chi^{(2)}$ interaction of few-cycle near infrared pulses in a PPLN crystal to generate optical frequency combs spanning 3 μm to 5.5 μm. The offset frequency, which is directly generated as a consequence of cascaded nonlinear processes, is stabilized with < 100 as precision. The frequency combs are subsequently used for broad bandwidth and high-resolution dual-comb spectroscopy with ppb sensitivity. Further, we have shown how to engineer the periodic poling to generate frequency combs with 40 THz bandwidth that support few-cycle MIR pulses. These pulses are interesting candidates for parametric amplification and further use in studying phenomena sensitive to the carrier-envelope phase [58].

*scott.diddams@nist.gov
†alexander.lind@colorado.edu
‡These authors contributed equally to this work.

[1] A. D. Ludlow, M. M. Boyd, J. Ye, E. Peik, and P. O. Schmidt, Rev. Mod. Phys. **87**, 637 (2015).

[2] A. Baltuška, T. Udem, M. Uiberacker, M. Hentschel, E. Goulielmakis, C. Gohle, R. Holzwarth, V. S. Yakovlev, A. Scrinzi, T. W. Hänsch, and F. Krausz, Nature (London) **421**, 611 (2003).

[3] A. Schliesser, N. Picqué, and T. W. Hänsch, Nat. Photonics **6**, 440 (2012).

[4] E. Baumann, F. R. Giorgetta, W. C. Swann, A. M. Zolot, I. Coddington, and N. R. Newbury, Phys. Rev. A **84**, 062513 (2011).

[5] J. Mulrooney, J. Clifford, C. Fitzpatrick, and E. Lewis, Sens. Actuators, A**136**, 104 (2007).

[6] L. M. Golston, L. Tao, C. Brosy, K. Schäfer, B. Wolf, J. McSpiritt, B. Buchholz, D. R. Caulton, D. Pan, M. A. Zondlo, D. Yoel, H. Kunstmann, and M. McGregor, Appl. Phys. B **123**, 170 (2017).

[7] A. Loh and M. Wolff, J. Quant. Spectrosc. Radiat. Transfer **203**, 517 (2017), HITRAN2016 Special Issue.

[8] L. Zhu et al., Atmos. Chem. Phys. **16**, 13477 (2016).

[9] D. G. Lancaster, A. Fried, B. Wert, B. Henry, and F. K. Tittel, Appl. Opt. **39**, 4436 (2000).

[10] B. J. Bjork, T. Q. Bui, O. H. Heckl, P. B. Changala, B. Spaun, P. Heu, D. Follman, C. Deutsch, G. D. Cole, M. Aspelmeyer, M. Okumura, and J. Ye, Science **354**, 444 (2016).

[11] A. J. Fleisher, B. J. Bjork, T. Q. Bui, K. C. Cossel, M. Okumura, and J. Ye, J. Phys. Chem. Lett. **5**, 2241 (2014).

[12] G. Clemens, J. R. Hands, K. M. Dorling, and M. J. Baker, Analyst **139**, 4411 (2014).

[13] K. Maquelin, C. Kirschner, L. P. Choo-Smith, N. van den Braak, H. P. Endtz, D. Naumann, and G. J. Puppels, J. Microbiol. Methods **51**, 255 (2002).

[14] R. Bhargava, Appl. Spectrosc. **66**, 1091 (2012).

[15] M. J. Walsh, R. K. Reddy, and R. Bhargava, IEEE J. Sel. Top. Quantum Electron. **18**, 1502 (2012).

[16] T. Popmintchev, M.-C. Chen, D. Popmintchev, P. Arpin, S. Brown, S. Ališauskas, G. Andriukaitis, T. Balčiunas, O. D. Mücke, A. Pugzlys, A. Baltuška, B. Shim, S. E. Schrauth, A. Gaeta, C. Hernández-García, L. Plaja, A. Becker, A. Jaron-Becker, M. M. Murnane, and H. C. Kapteyn, Science **336**, 1287 (2012).

[17] B. Wolter, M. G. Pullen, M. Baudisch, M. Sclafani, M. Hemmer, A. Senftleben, C. D. Schröter, J. Ullrich, R. Moshammer, and J. Biegert, Phys. Rev. X **5**, 021034 (2015).

[18] S. Ghimire and D. A. Reis, Nat. Phys. **15**, 10 (2019).

[19] N. Leindecker, A. Marandi, R. L. Byer, K. L. Vodopyanov, J. Jiang, I. Hartl, M. Fermann, and P. G. Schunemann, Opt. Express **20**, 7046 (2012).

[20] F. Adler, K. C. Cossel, M. J. Thorpe, I. Hartl, M. E. Fermann, and J. Ye, Opt. Lett. **34**, 1330 (2009).

[21] K. Balskus, Z. Zhang, R. A. McCracken, and D. T. Reid, Opt. Lett. **40**, 4178 (2015).

[22] A. V. Muraviev, V. O. Smolski, Z. E. Loparo, and K. L. Vodopyanov, Nat. Photonics **12**, 209 (2018).

[23] Y. Jin, S. M. Cristescu, F. J. M. Harren, and J. Mandon, Appl. Phys. B **119**, 65 (2015).

[24] D. D. Hickstein, H. Jung, D. R. Carlson, A. Lind, I. Coddington, K. Srinivasan, G. G. Ycas, D. C. Cole, A. Kowligy, C. Fredrick, S. Droste, E. S. Lamb, N. R. Newbury, H. X. Tang, S. A. Diddams, and S. B. Papp, Phys. Rev. Applied **8**, 014025 (2017).

[25] N. Nader, D. L. Maser, F. C. Cruz, A. Kowligy, H. Timmers, J. Chiles, C. Fredrick, D. A. Westly, S. W. Nam, R. P. Mirin, J. M. Shainline, and S. Diddams, APL Photonics **3**, 036102 (2018).

[26] H. Guo, C. Herkommer, A. Billat, D. Grassani, C. Zhang, M. H. P. Pfeiffer, W. Weng, C.-S. Brès, and T. J. Kippenberg, Nat. Photonics **12**, 330 (2018).

[27] R. K. W. Lau, M. R. E. Lamont, A. G. Griffith, Y. Okawachi, M. Lipson, and A. L. Gaeta, Opt. Lett. **39**, 4518 (2014).

[28] F. C. Cruz, D. L. Maser, T. Johnson, G. Ycas, A. Klose, F. R. Giorgetta, I. Coddington, and S. A. Diddams, Opt. Express **23**, 26814 (2015).

[29] C. Erny, K. Moutzouris, J. Biegert, D. Kühlke, F. Adler, A. Leitenstorfer, and U. Keller, Opt. Lett. **32**, 1138 (2007).

[30] G. Ycas, F. R. Giorgetta, E. Baumann, I. Coddington, D. Herman, S. A. Diddams, and N. R. Newbury, Nat. Photonics **12**, 202 (2018).

[31] M. Yan, P.-L. Luo, K. Iwakuni, G. Millot, T. W. Hänsch, and N. Picqué, Light Sci. Appl. **6**, e17076 (2017).

[32] A. Hugi, G. Villares, S. Blaser, H. C. Liu, and J. Faist, Nature (London) **492**, 229 (2012).

[33] M. Piccardo, P. Chevalier, S. Anand, Y. Wang, D. Kazakov, E. A. Mejia, F. Xie, K. Lascola, A. Belyanin, and F. Capasso, Appl. Phys. Lett. **113**, 031104 (2018).

[34] S. Barbieri, M. Ravaro, P. Gellie, G. Santarelli, C. Manquest, C. Sirtori, S. P. Khanna, E. H. Linfield, and A. G. Davies, Nat. Photonics **5**, 306 (2011).

[35] T. Hu, S. D. Jackson, and D. D. Hudson, Opt. Lett. **40**, 4226 (2015).

[36] O. Henderson-Sapir, J. Munch, and D. J. Ottaway, Opt. Lett. **39**, 493 (2014).

[37] S. Duval, M. Bernier, V. Fortin, J. Genest, M. Piché, and R. Vallée, Optica **2**, 623 (2015).

[38] M. Yu, Y. Okawachi, A. G. Griffith, M. Lipson, and A. L. Gaeta, Optica **3**, 854 (2016).

[39] H. Timmers, A. Kowligy, A. Lind, F. C. Cruz, N. Nader, M. Silfies, G. Ycas, T. K. Allison, P. G. Schunemann, S. B. Papp, and S. A. Diddams, Optica **5**, 727 (2018).

[40] A. S. Kowligy, A. Lind, D. D. Hickstein, D. R. Carlson, H. Timmers, N. Nader, F. C. Cruz, G. Ycas, S. B. Papp, and S. A. Diddams, Opt. Lett. **43**, 1678 (2018).

[41] A. Sell, R. Scheu, A. Leitenstorfer, and R. Huber, Appl. Phys. Lett. **93**, 251107 (2008).

[42] I. Coddington, N. Newbury, and W. Swann, Optica **3**, 414 (2016).

[43] N. R. Newbury, I. Coddington, and W. Swann, Opt. Express **18**, 7929 (2010).

[44] I. Pupeza, D. Sánchez, J. Zhang, N. Lilienfein, M. Seidel, N. Karpowicz, T. Paasch-Colberg, I. Znakovskaya, M. Pescher, W. Schweinberger, V. Pervak, E. Fill, O. Pronin, Z. Wei, F. Krausz, A. Apolonski, and J. Biegert, Nat. Photonics **9**, 721 (2015).

[45] C. Gaida, M. Gebhardt, T. Heuermann, F. Stutzki, C. Jauregui, J. Antonio-Lopez, A. Schülzgen, R. Amezcua-Correa, A. Tünnermann, I. Pupeza, and J. Limpert, Light Sci. Appl. **7**, 94 (2018).

[46] O. Novák, P. R. Krogen, T. Kroh, T. Mocek, F. X. Kärtner, and K.-H. Hong, Opt. Lett. **43**, 1335 (2018).

[47] S. Vasilyev, I. Moskalev, M. Mirov, V. Smolski, S. Mirov, and V. Gapontsev, Opt. Mater. Express **7**, 2636 (2017).

[48] A Catanese, J. Rutledge, M. C. Silfies, X. Li, H. Timmers, A. S. Kowligy, A. Lind, S. A. Diddams, and T. K. Allison, Opt. Lett. **45**, 1248 (2020).

[49] T. Fuji, J. Rauschenberger, A. Apolonski, V. S. Yakovlev, G. Tempea, T. Udem, C. Gohle, T. W. Hänsch, W. Lehnert, M. Scherer, and F. Krausz, Opt. Lett. **30**, 332 (2005).

[50] A. S. Kowligy, H. Timmers, A. J. Lind, U. Elu, F. C. Cruz, P. G. Schunemann, J. Biegert, and S. A. Diddams, Sci. Adv. **5**, eaaw8794 (2019).

[51] G. Genty, P. Kinsler, B. Kibler, and J. M. Dudley, Opt. Express **15**, 5382 (2007).

[52] M. Conforti, F. Baronio, and C. De Angelis, Phys. Rev. A **81**, 053841 (2010).

[53] M. Charbonneau-Lefort, B. Afeyan, and M. M. Fejer, JOSA B **25**, 1402 (2008).

[54] P. E. Powers, T. J. Kulp, and S. E. Bisson, Opt. Lett. **23**, 159 (1998).

[55] S. W. Sharpe, T. J. Johnson, R. L. Sams, P. M. Chu, G. C. Rhoderick, and P. A. Johnson, Appl. Spectrosc. **58**, 1452 (2004).

[56] L. S. Rothman et al., J. Quant. Spectrosc. Radiat. Transfer **130**, 4 (2013), HITRAN2012 special issue.

[57] B. Spaun, P. B. Changala, D. Patterson, B. J. Bjork, O. H. Heckl, J. M. Doyle, and J. Ye, Nature (London) **533**, 517 (2016).

[58] T. Rybka, M. Ludwig, M. F. Schmalz, V. Knittel, D. Brida, and A. Leitenstorfer, Nat. Photonics **10**, 667 (2016).